

HIGHLY TEXTURED (001) AlN NANOSTRUCTURED THIN FILMS SYNTHESIZED BY REACTIVE MAGNETRON SPUTTERING FOR SAW AND FBAR APPLICATIONS

G. E. STAN*, I. PASUK, A. C. GALCA, A. DINESCU^a

National Institute of Materials Physics, P.O. Box MG-7, Bucharest-Magurele, 077125, Romania

^a *IMT-Bucharest, 32B, Erou Iancu Nicolae street, Bucharest 077190, Romania*

Highly oriented (001) AlN (wurtzite type) thin films have been successfully deposited on silicon, platinized silicon and glass substrates by reactive radio-frequency magnetron sputtering at low temperature (150°C). X-ray diffraction, spectroscopic ellipsometry and scanning electron microscopy techniques have been employed to assess the structural characteristics of the AlN films. We have investigated both the influence of AlN film's thickness and of the substrate nature on crystallinity. The thicker films present a better c axis alignment, a minimum orientation dispersion of 3.5° being reached for 1 μm AlN on silicon. The micro- and macrostrain of the AlN lattice relaxes as the film thickness increases. The film deposited onto platinum has the maximum value of tensile strain along c axis. The film on glass exhibited the poorest texturing and the highest defect concentration. From an optical point of view the film deposited on Pt is the denser one and that deposited on glass is the most rarefied. One can conclude that when using a low deposition temperature and a base pressure of ~10⁻⁴ Pa the increase of film thickness leads to improved AlN structure on Si or Pt supports.

(Received November 12, 2010; accepted November 22, 2010)

Keywords: AlN films, magnetron reactive sputtering, texture, microstrain, optical properties

1. Introduction

In the last years, the development of wide band gap (WBG) semiconductor processing technologies has opened the perspective of manufacturing surface acoustic wave (SAW) and film bulk acoustic resonator (FBAR) devices for application in the GHz frequency range. The 4G mobile communication systems are expected to work within the 3–6 GHz range [1,2]. Among the WBG materials, the aluminium nitride (AlN), a III–V compound semiconductor, is of great technological interest due to its exceptional properties such as wide energy band gap (6.2 eV), high breakdown voltage, high electrical resistivity (~10¹⁵ ohm·cm), high hardness (11–15 GPa), high piezoelectric coupling factor, good chemical and thermal stability, high thermal conductivity, and high surface acoustic velocity (up to 6000 m/s) [3–5]. Among the nitrides AlN has the largest piezoelectric coefficients and the higher corrosion resistance [4]. Highly c-axis oriented AlN thin films are attractive for many acoustic and optic applications: micro-electromechanical (MEMS) and nano-electromechanical (NEMS) devices, high-power and high-temperature electronic devices and optoelectronic devices at the ultraviolet region [4,6]. The MEMS and NEMS resonators are regarded as promising technologies for many hi-tech applications (electrometry, chemical and biological sensing, and scanning probe techniques) [6].

In order to develop better acoustic devices, a wide range of deposition methods have been employed with the aim of growing highly oriented AlN thin films, including chemical vapour

* Corresponding author: george_stan@infim.ro

deposition [7], molecular beam epitaxy [8], metal organic chemical vapour deposition [9], hydride vapour phase epitaxy [10], pulsed laser deposition [11,12] and direct current (DC) and radio-frequency (RF) magnetron sputtering [13–15]. Among all the techniques, RF reactive magnetron sputtering technique has emerged as an easily applicable method for preparing AlN films with preferred crystal orientations and reduced roughness at low pressure and temperatures [14].

Recently, in our research group, efforts have been made for obtaining high quality AlN films onto high resistivity silicon by RF reactive magnetron sputtering, which lead to successfully development of FBAR and SAW devices with excellent performances [1,2,16]. Resonance frequencies of about 10 GHz for FBAR structures [2] and of about 5 GHz for the SAW devices [16] have been obtained. The best previous result found in literature was a SAW on AlN (but on diamond not on silicon) operating at 4.5 GHz [17].

It is well-known that the characteristics of AlN thin films are greatly influenced by their microstructure. Our study attempts to offer a comprehensive insightful structural view of these highly c-axis oriented AlN layers. In this work AlN/Si layers were grown on different substrates by RF reactive magnetron sputtering, varying the deposition time, in order to investigate the films' growth architecture, the films' quality versus thickness and their behaviour in ambient media, for future development of acoustic devices designs. Extensive micro-structural and optical measurements have been performed on the sputtered AlN films in this regard.

2. Experimental

2.1 Deposition procedure

The AlN films were synthesized using a UVN-75R1 sputtering deposition system equipped with planar water-cooled magnetron cathodes (110 mm diameter). An aluminum disc (Mateck GmbH, 99.99 % purity, 3 mm thick) was used as a cathode target. Silicon (100) wafers, Corning 1737 glass and platinized silicon [Pt(100nm)/TiO₂(15nm)/SiO₂(450nm)/Si] wafers were used as substrates. Before the introduction into the deposition chamber, the substrates were successively cleaned ultrasonically in acetone and ethanol for 10 min in a NAHITA 610/6 ultrasonic bath. The target-to-substrate distance was set at 30 mm. In a first step, the sputtering chamber was evacuated down to a base pressure of 10⁻⁴ Pa. Further on, high purity argon (99.99%) was introduced through a needle valve and the gas flow was maintained at a value of 40 sccm. The target was sputter-cleaned at a working pressure of 0.3 Pa for 15 minutes to remove surface contaminants. During cleaning, the substrates were masked with a stainless steel shield in order to avoid undesired depositions onto the substrates' surface. Prior to deposition, the substrates were etched for 10 min, at a 0.4 kV DC bias voltage in argon plasma produced by a wolfram plasmatron, in order to remove the thin native oxide layers and other impurities which might persist after the ultrasonic cleaning. This substrates' treatment is known to increase films' adhesion and reduce the possibility of delamination phenomena [18].

We used a radio-frequency (1.78 MHz) generator and maintained a constant and low RF power (100 W) in order to avoid overheating of the target surface. A plasma ring of about 55 mm diameter was generated by the planar magnetron cathode. Films with thickness of 0.2, 0.75 and 1 μm were deposited at a sputtering rate of 12.5 nm/min in 0.2 Pa Ar-N₂ gas mixture with a nitrogen concentration of 25%. The substrates were not heated during deposition and their temperature was only dependent on plasma self-heating. During deposition the substrates reached a maximum temperature of ~150°C as monitored with a built-in Chromel-Alumel thermocouple system.

2.2 Characterization of AlN sputtered films

a) X-ray Diffraction (XRD)

The crystallographic structure of each film was analyzed by X-ray diffraction (XRD) on a Bruker-AXS D8 Advance diffractometer in parallel beam setting, with monochromatized CuK_{α1}

radiation. Diffraction data were collected in symmetric (θ - θ) geometry, in asymmetric (2θ - ω) geometry in order to acquire information through planes tilted to the surface, and through rocking curves.

b) Spectroscopic Ellipsometry (SE)

For optical characterization, we use a *Woollam V-VASE* (Vertical – Variable Angle Spectroscopic Ellipsometer) system. Measurements are performed in the visible and near-ultraviolet region of the spectrum at energies between 0.7 and 4.5 eV at 45° , 60° and 75° .

c) Scanning Electron Microscopy (SEM)

The growth morphology of the films was examined using scanning electron microscopy (*FEI Nova NanoSEM 630*; 5 kV acceleration voltage and 10 μ A beam current) under secondary electron mode, in cross-view mode.

3. Results

3.1 XRD results

The XRD measurements have firstly to ascertain the right crystallo-chemical structure of the AlN films. Due to the highly textured growth, in case of all films there are only two diffraction lines originating from the film in the whole accessible scanning range (Figure 1). These peaks can be associated either to the (001) planes of hexagonal AlN (ICDD # 79-2497), that diffract at $2\theta = 35.9^\circ$ (002) and $2\theta = 76.1^\circ$ (004), or to the (111) planes of cubic AlN (ICDD # 80-10) diffracting at $2\theta = 35.6^\circ$ (111) and $2\theta = 75.4^\circ$ (222). In order to solve this non trivial problem we searched for characteristic diffraction peaks of tilted planes, performing asymmetric scans. The only accessible planes for the given instrumental setting were: (103) of hexagonal AlN (tilt angle $\tau = 31.6^\circ$, diffraction angle $2\theta = 66.1^\circ$), and (113) of cubic AlN (tilt angle: $\tau = 29.5^\circ$, diffraction angle: $2\theta = 71.6^\circ$). We have found the hexagonal AlN (103) peaks, proving the highly *c*-axis textured hexagonal structure of the AlN films. Only the film deposited on glass exhibits several other peaks of hexagonal AlN, but showing as well a rather strong *c*-axis preferred orientation (Figure 1). It is to note that the intensity diffracted by this film is comparable to that of the thinnest film onto Si, despite its thickness is almost four times greater, suggesting that the crystallization did not occurred in the whole volume.

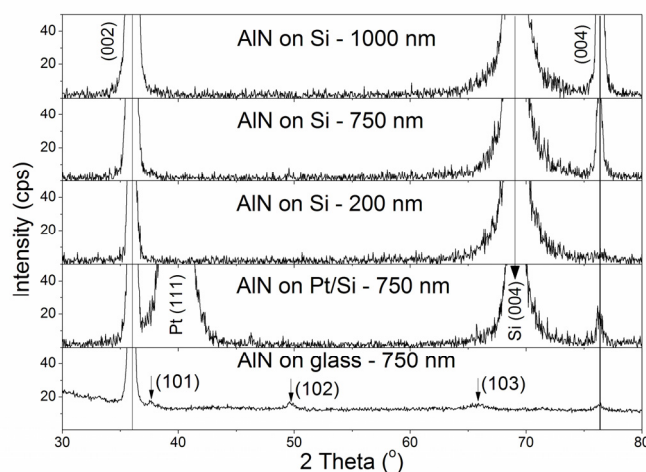


Fig. 1. The XRD patterns of the analyzed samples

Because many applications of AlN are related to texture, the determination of the degree of orientation is of great interest. In order to determine quantitatively the degree of misalignment of the AlN (001) planes, rocking curves were recorded using the 002 reflection (Figure 2). The full width at half maximum of these curves is a measure of the c -axis orientation dispersion.

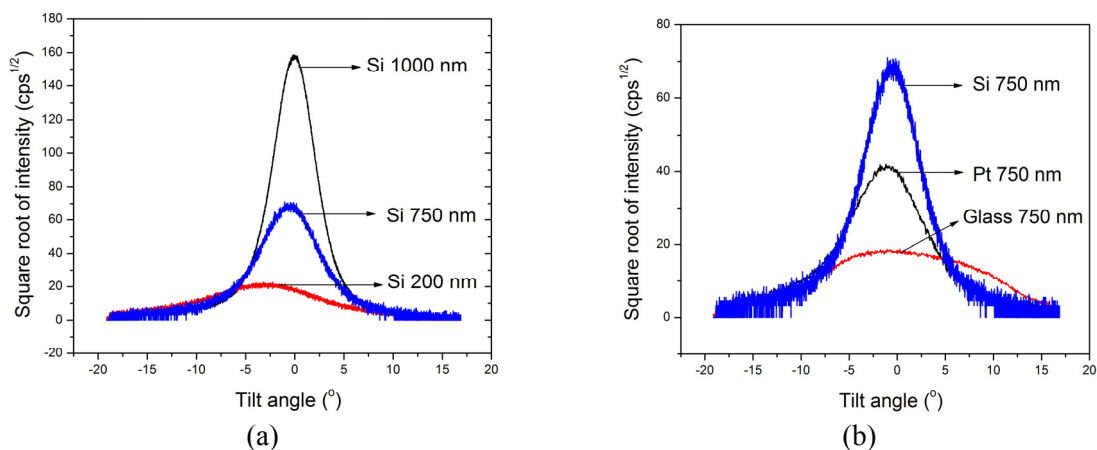


Fig. 2. Rocking curves of AlN (001) planes represented as centred on zero; comparative representation for films with different thicknesses on Si (a), and for films with the same thickness on different substrates (b)

Figure 3 shows that the degree of misalignment decreases with the increase of film thickness on silicon, in an almost linear dependence, reaching a minimum of 3.5° for the 1 μm thick film. The film deposited onto Pt approaches the value of that on Si with the same thickness, while the film on glass, having the same thickness, have much larger orientation dispersion, as it has been revealed also by the θ - θ scan (Figure 1). A piezoelectric response can be obtained in AlN with rocking curve FWHM up to $\sim 10^\circ$, but it is desirable for this value to be as low as possible.

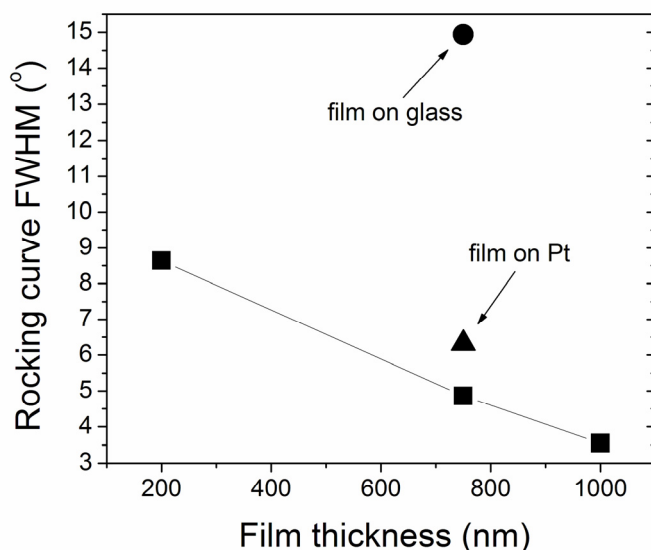


Fig. 3. Dispersion of AlN c axis alignment, determined from rocking curves

Another important parameter for the functionality of AlN films is the internal stress. The atomic structure of the substrate influences the structure of the film with which it is in contact, and the structure of the growing crystallites. The accommodation of the AlN (001) planes in contact with the substrate implies modifications of the interatomic distances, leading to local modifications of the interplanar distances. Strain can be also induced by ion bombardment during sputtering. The strain, expressed as $\epsilon = \Delta d/d$, may be non-uniform within a crystallite (microstrain), so that different parts of the material diffracts at slightly different angles, producing line broadening. Therefore the

strain broadening of the diffraction lines is related to the dispersion, $\langle \varepsilon^2 \rangle^{1/2}$. The microstrain is associated with the local defect structure of the lattice, such as disorder at the interface or crystallite boundaries, and dislocations. If the average strain over the whole volume of the film in the X-ray beam is non-vanishing (macrostrain), it results in shifts of the diffraction peaks. The macrostrain can be of elongation or of compression. The degrees of deformation of a crystallite in different directions are related through the elastic characteristics of the material.

The macrostrain normal to the surface was determined as:

$$\varepsilon_{\perp} = (c - c_0) / c_0 \quad (1)$$

where c resulted from the positions of 002 and 004 reflections, and $c_0 = 4.978 \text{ \AA}$ is the c axis period of the unstrained sample (ICDD # 79-2497). The results presented in Figure 4 show a tensile strain normal to the surface for all of the investigated AlN films. The AlN lattice is the most strained on Pt substrate, and is the most relaxed in the thickest film on Si.

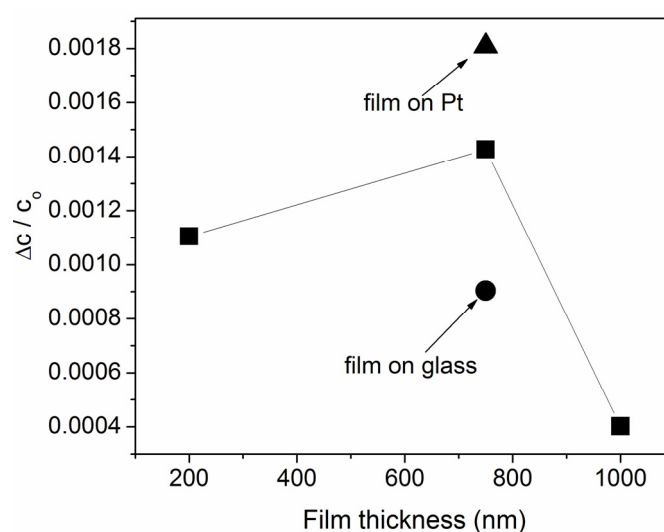


Fig. 4. Macrostrain normal to the surface, ε_{\perp} , vs. film thickness and substrate materials

The microstrain was determined from the line broadening. The diffraction line broadening is generally a combined effect of the small crystallite size and microstrain. In the present paper we tried to determine the microstrain using the Williamson-Hall (WH) method that assumes the additivity of these two integral breadth components, resulting in the relation:

$$\beta \cos \theta = \frac{\lambda}{L} + \langle \varepsilon^2 \rangle^{1/2} \sin \theta \quad (2)$$

where β is the integral breadth corrected for the instrumental line breadth, L is the average crystallite size (coherence length) normal to the crystal planes considered, θ is the diffraction angle, and λ is the X-ray wavelength [19]. The instrumental line width was determined by using a heat treated ceria powder, proved to have no strain or size line broadening. In order to determine the line breadths detailed scans of the available diffraction peaks of the AlN films were performed (Figure 5).

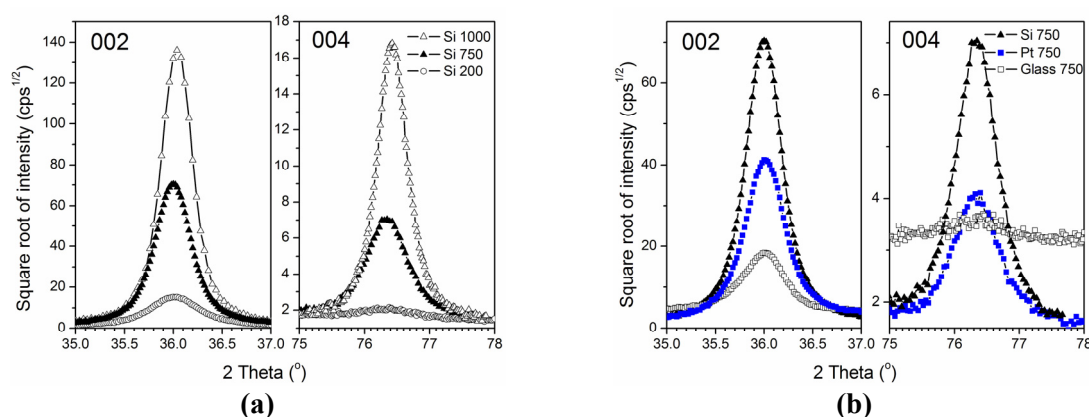


Fig. 5. Peak profile details; comparative representation for films with different thicknesses on Si (a), and for films with the same thickness on different substrates (b)

Despite the long collection times, the 004 peaks of the thinnest film on Si and of the AlN on glass are very noisy, providing large experimental errors. The line profiles were fitted with using split pseudo-Voigt profiles. The WH plots are presented in Figure 6. The error bars were estimated by error propagation laws starting from the errors of the profile parameters provided by the fitting routine.

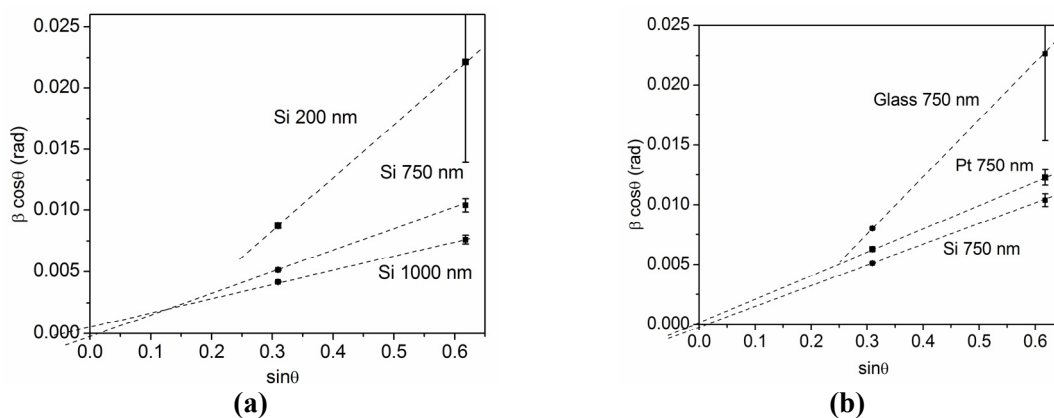


Fig. 6. WH plots; comparative representation for films with different thicknesses on Si (a), and for films with the same thickness on different substrates (b)

The straight lines were extrapolated to the origin aiming to estimate the crystallite sizes from the intercept $=\lambda/L$. The graphs of Si 1000 nm, Si 750 nm and Pt 750 nm intersect the ordinate near to the origin, suggesting that the crystallite size normal to the surface is so large that it does not contribute to the line broadening, being of the order of a micron. This suggests that the average crystallite height in these films equals the film's thickness. The plots for the thinnest AlN film on Si and for the incompletely crystallized film on glass look strange, showing very large slopes and with no physical meaning of the ordinates at the origin. Although the errors concerning the 004 peak of these films are very large, these data were not rejected, supposing they carry an information that can not be modelled by the integral breadths additivity assumed by the Williamson-Hall plot. Additional line broadening sources are suspected that should be properly extracted. However it is to note that the slopes of these lines are almost equal, showing the similarity of these two films from XRD point of view. The microstrains extracted from the slopes are represented vs. thickness and substrate materials in Figure 7.

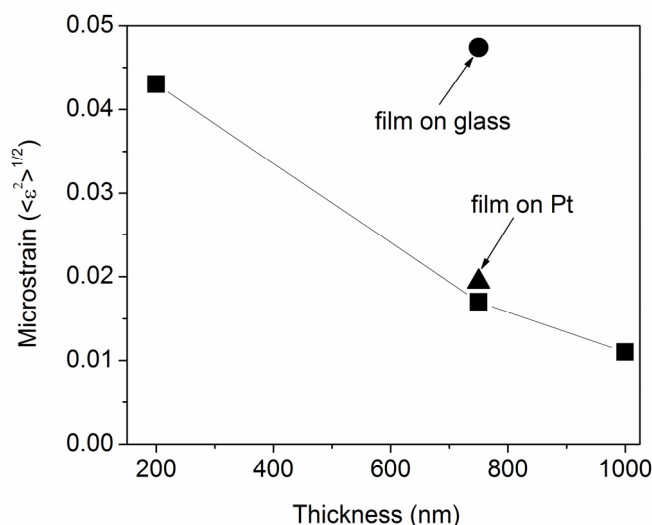


Fig. 7. Microstrains extracted from the WH plots

As only two reflections were available for the plots, the results should be considered rather qualitative, just to compare the films with each other. The microstrain decreases with thickness for the AlN film deposited onto Si, suggesting that the lattice defects at the interface are preponderant to those induced by ion bombardment. The AlN on glass shows the highest degree of lattice disorder, while that on Pt behaves similar as that with the same thickness deposited on Si.

It is interesting to observe the strong similitude between Figures 7 and 3, and one can infer that there is a correlation between the c axis misalignment and microstrain. The graph of rocking curve FWHM vs. microstrain comprising all the AlN films investigated is represented in Figure 8.

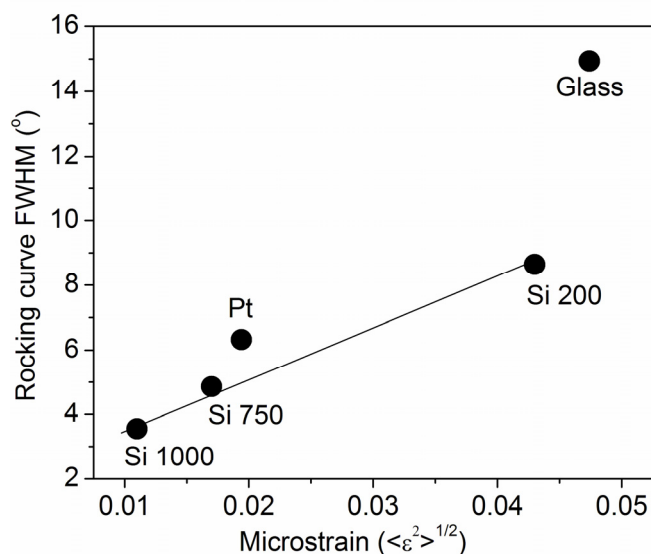


Fig. 8. The dependence of c axis misalignment on microstrain

Indeed, these two structural parameters seem to be in close relationship especially as regards the AlN film with different thicknesses on silicon, as if the main source of c axis misalignment is the defect structure within the crystallites. Since the film is built up of columnar crystallites whose height is of the order of the film thickness, one can draw the conclusion that the misalignment is caused by dislocations which introduce a “local tilt” of c axis, and a local perturbation of the lattice, without leading to the break the crystallites (coherence length).

The diffraction lines of the tilted AlN (103) plane, presented in Figure 9, have been used to draw out structural information related to the in-plane structure. It is to note the splitting in case of the film deposited onto Pt substrate. This could be related to the local epitaxy of AlN on Pt

(111) in early stage of the AlN growth, but this is beyond the subject of the present paper. The data reported hereinafter refers to the left peak which fit well with the 103 peak of the other analyzed films.

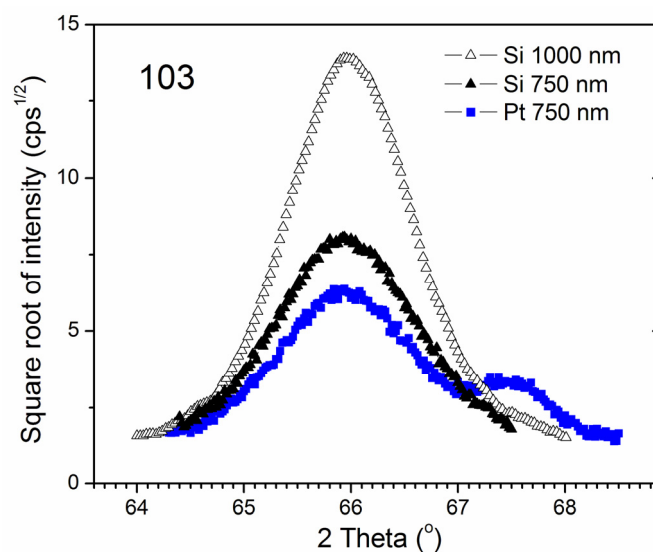


Fig. 9. Asymmetric 2θ - ω scan of the tilted (103) planes

The 103 peak breadth is sensible larger than that of the 004 peak for all films, suggesting a size anisotropy of the AlN crystallites. Supposing that the microstrain is isotropic, one can use the 103 line broadening to estimate the mean crystallite size in a direction normal to the (103) planes, L_{103} , using the WH method. This can be made by graphical means, by drawing a straight line through the point corresponding to the 103 point in the WH plot, with the same slope as of the line drawn by the points corresponding to 002 and 004 peaks of the given AlN film; the ordinate at origin is λ/L_{103} (Figure 10).

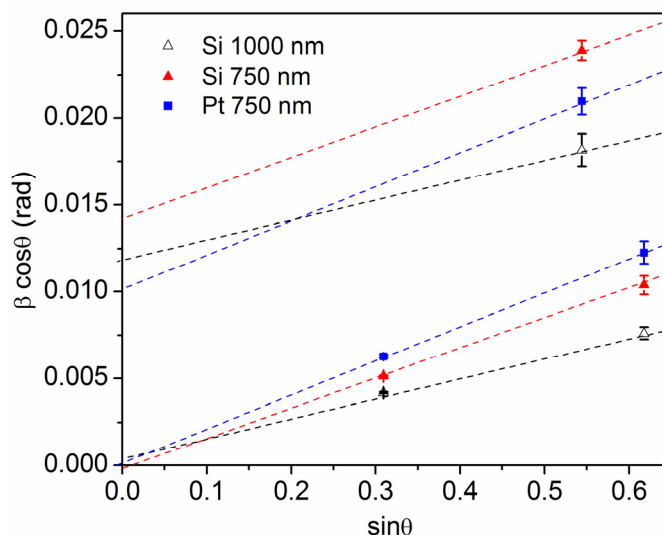


Fig. 10. WH plot for estimation of the mean crystallite size perpendicular to the (103) planes, by assuming the same microstrain as obtained in a direction normal to the surface

Furthermore, knowing the tilt angle one can estimate the crystallite size in a direction parallel to the surface, $L_{\parallel}=L_{103} \cos(90-\tau)$. The results are presented in Table 1:

Table 1. Lateral coherence lengths obtained by WH method on the basis of the 103 line broadening

Sample	L_{103} (nm)	$L_{ }$ (nm)
Si 1000 nm	10.8	5.4
Si 750 nm	13.0	6.5
Pt 750 nm	14.1	7.0

The extremely small values of $L_{||}$ might indicate that the strain contribution to the line broadening was under-estimated, this being larger than in direction normal to the surface.

3.2 SE measurements

Spectroscopic ellipsometry is used to evaluate the optical properties of AlN thin films obtained on different substrates. In ellipsometry, the change of the polarization state of linearly polarized light is measured upon reflection at the surface. The complex reflection coefficient ρ is defined as [20,21]:

$$\rho = \frac{\tilde{R}_p}{\tilde{R}_s} = \tan(\Psi)e^{j\Delta} \quad (3)$$

where \tilde{R}_p and \tilde{R}_s are the reflection coefficients for the parallel and perpendicular polarizations, respectively. Historically, the quantity ρ is expressed in the two angles Ψ and Δ , inserted in the above expression.

An accurate model is required for the system under consideration, which enables simulation or fitting of the results. The spectra were analyzed by using a two layer model (substrate and thin film) in all cases. Since the 100 nm Pt layer is opaque in the measured spectral range, it can be regarded as substrate. In these models the physical parameters are the thin film thickness and its dielectric function. The optical properties are expressed by dielectric function ε or by the complex refractive index $\tilde{\mathbf{n}}$ which are related by:

$$\varepsilon \equiv \varepsilon_1 - j\varepsilon_2 \equiv \tilde{\mathbf{n}}^2 \equiv (n - jk)^2 \quad (4)$$

When the extinction coefficient k is zero, the refractive index (a real number) will be the square root of ε , also a real number.

In this paper, two approaches were used to assess the optical properties of the obtained thin films. The first approach is to model the refractive index in the spectral range where the films are transparent ($k=0$) by using a Cauchy dispersion [22, 23]:

$$n(\lambda) = A + \frac{B}{\lambda^2} + \frac{C}{\lambda^4} + \dots \quad (5)$$

where A, B and C are specific material parameters.

In the spectral range where the extinction coefficient k is zero, the refractive index of a single crystal material is larger than the refractive index of polycrystalline or amorphous counterparts. The electric polarization is directly responsible for defining the refractive index in the visible spectral range. Since this polarization is dependent on the atomic density [20], a lighter material will have a smaller refractive index. Therefore, missing atoms, less dense grain boundaries or a rarefied amorphous-like structure, lower the density of the basic single crystal. With this respect, a thin film can be regarded as a single crystal material with embedded small voids. For this model, a Bruggeman effective medium approximation is used [21,24]:

$$0 = f_{AIN} \frac{\epsilon_{AIN} - \epsilon_{eff}}{\epsilon_{AIN} + 2\epsilon_{eff}} + (1 - f_{AIN}) \frac{\epsilon_{air} - \epsilon_{eff}}{\epsilon_{air} + 2\epsilon_{eff}} \quad (6)$$

where ϵ_{AIN} , $\epsilon_{air}=1$ and ϵ_{eff} are the dielectric function of AlN crystal [25], of air and of obtained thin film; f_{AIN} is the fill fraction of AlN component.

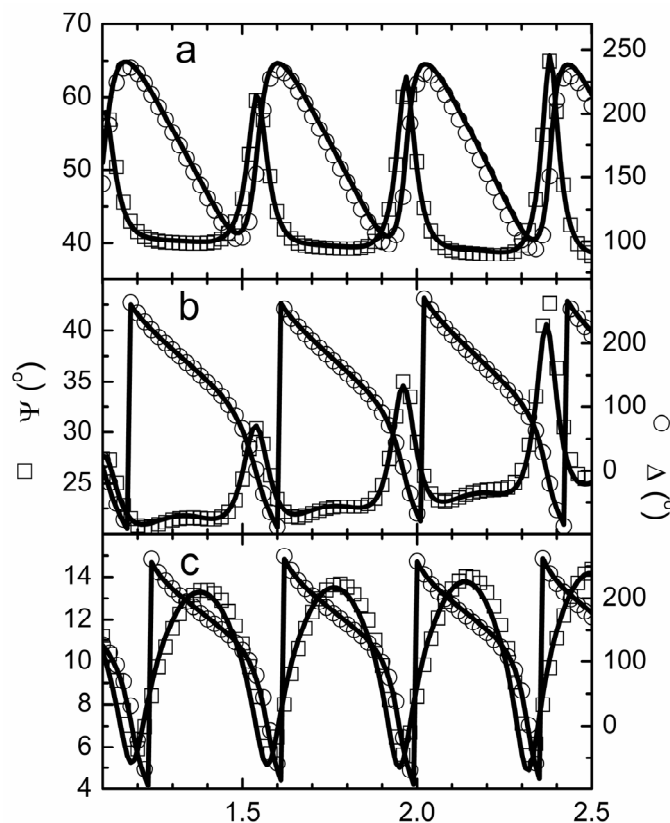


Fig. 11. Ellipsometry spectra for aluminium nitride films acquired at an angle of incidence of 60° , on Pt (a), Si (b) and glass (c). The open symbols represent experimental data, while the solid lines are obtained from a fitting procedure using the EMA model described in the text

In Figure 11 are presented the experimental ellipsometry spectra and the generated ones by using a 2 layer model and an EMA approximation of the deposited thin film. In all cases is observed a good match between experimental and theoretical spectra. The results are presented in the table below.

Table 2. Parameters fitted by using the two presented models. The errors are those given by the fitting routine.

Substrate	Thickness (nm)		$(1 - f_{AIN})$ (%)	n @ 630nm	
	Cauchy	EMA		Cauchy	EMA
Pt	724.16 ± 0.8	729.06 ± 2.4	5.50 ± 0.48	2.100	2.087
Si	756.01 ± 0.5	756.58 ± 0.7	6.96 ± 0.12	2.072	2.070
Glass	840.67 ± 0.6	841.99 ± 0.8	6.17 ± 0.13	2.083	2.079

Both models give approximately the same values of thickness and refractive index. If it is assumed that for the same deposition time, equal number of atoms reaches the surface and contributes into thin film growing, is observed that on the Pt substrate the film is more compact (dense), while on glass, the highest thickness is correlated with the most rarefied thin film. A question mark appears regarding the voids fill fraction, which describes qualitatively the optical density of deposited thin films compared with a bulk single crystal. This contradiction can be

explained by the contribution of interaction between polarized atoms, and therefore for a quasi-amorphous structure the above mentioned effective medium approximation is poor.

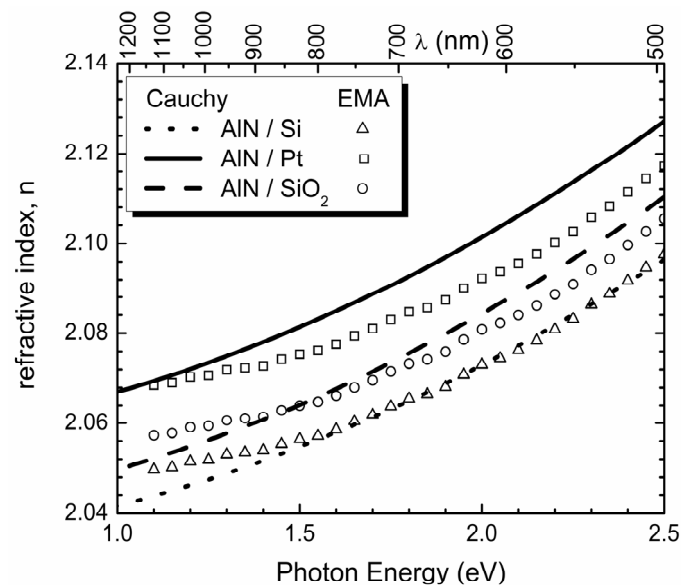


Fig. 12. Refractive index dispersions of aluminium nitride films on different substrates. The lines represent the Cauchy dispersions, while the symbols are the EMA dispersions

In Figure 12 are presented the refractive indices of obtained thin films. Both models used give similar dispersions. Also the refractive index of AlN deposited on Platinum substrates is the largest one, while the one of AlN deposited on Silicon is the smallest one.

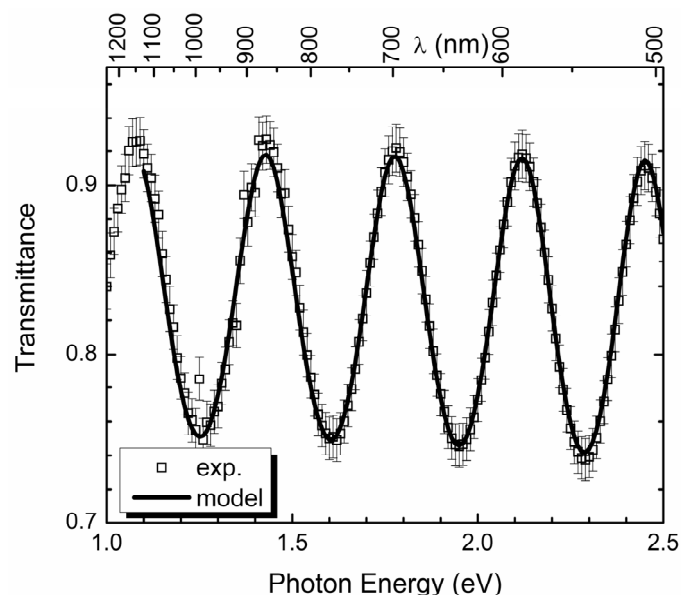


Fig. 13. Transmittance spectrum through the AlN/glass sample. The open squares represent the experimental data, while the line is generated using the EMA model used in ellipsometry data analysis

In Figure 13 is presented the conventional transmission spectrum of AlN deposited on Corning glass substrate. If it is used the ellipsometry model with the same parameters, thickness and refractive index, and a transmission is generated, then an identical spectrum is obtained.

3.3 SEM analysis

The cross-sectional SEM view presented in Figure 14 showed that both AlN films deposited on Si (100) substrates for 16 and 80 minutes, respectively, exhibit a well-developed columnar grain structure. Also, the films' thicknesses estimated from these micrographs correspond to the ones estimated by SE measurements.

A more compact microstructure was noticed for the thicker (1 μm) AlN film (Figure 14-b), in good correlation with the XRD results. One can suppose that in the first stages of deposition, the growing AlN film is formed both by well-textured regions and randomly ordered regions, due to an initial instability of AlN nucleation, and further growth processes. At low sputtering pressures, such as the one used in this study (0.2 Pa), the mean free paths of the sputtered particles increase along with their kinetic energy due the minimization of detrimental processes such as particle scattering due collisions or thermalization phenomena [15,26,27]. In these conditions, the atoms arrive at the substrate with higher energy and also the particles in the magnetron plasma can easily deliver their kinetic energy to the ad-atoms at the growing film surface. It is generally considered that the basal plane in hexagonal structures has the lowest surface energy and the maximum atomic density, therefore favourable for Al and N atoms' rearrangement [13,15,28].

The difference in film's compactness might be due to different growth rates of textured regions with respect to the randomly oriented ones [13,28]. Moreover, the bombardment at the growing film's surface with atoms with high enough energy could cause the film's densification by decreasing the voided regions in the microstructure, since atoms with sufficient kinetic energy at the film surface may rearrange themselves in energetic-favoured planes, under certain thermal equilibrium conditions. In time, well-textured regions are formed, and they keep growing and spread, the film becoming more homogeneous. The longer the deposition time, the well developed is the crystalline structure over the whole film volume, and the higher the texturing is, as confirmed by XRD. The (002) well-textured regions are growing faster, at the expense of the randomly oriented ones. As a result, after a certain amount of time the well-textured region become dominant, highly (001) oriented AlN films with columnar texture being obtained.

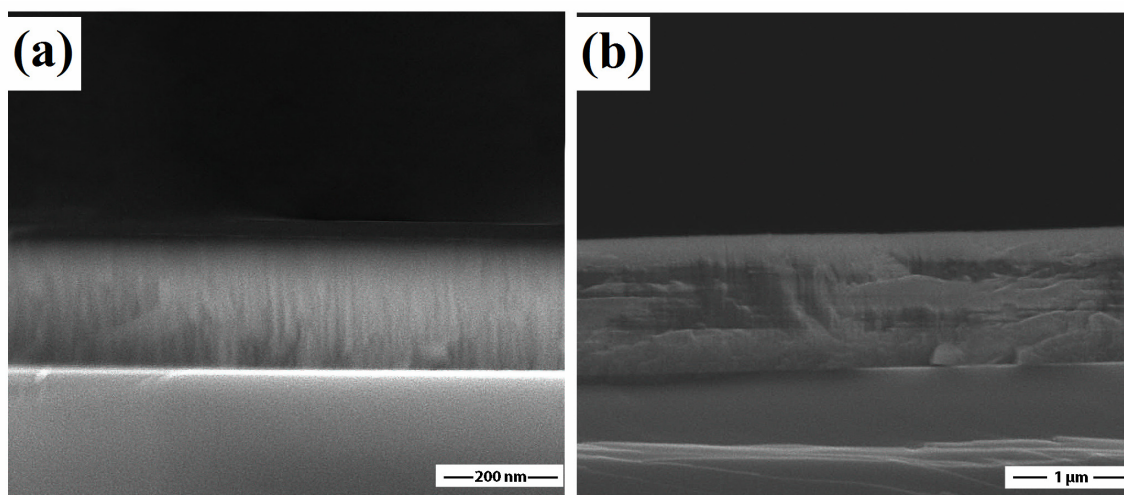


Fig. 14. Cross-view SEM micrographs of AlN reactive sputtered films onto silicon substrates: (a) 16 minutes ~ 200 nm; (b) 80 minutes ~ 1 μm

4. Conclusions

The paper present a technological algorithm for successfully preparing highly c-axis oriented aluminium nitride films by reactive sputtering, suitable for SAW and FBAR applications. Insightful structural and optical studies were presented, aiming to understand on the one hand the physical processes implied in AlN films' growth, and on the other hand the dependence of various structural and optical parameters on film thickness and deposition substrate. The alignment of the

crystalline planes is better for thicker films, reaching a minimum dispersion of 3.5° for the 1 micron thick AlN film on Si (100) substrate. The crystallites seem to be needle-shaped, with heights comparable to the film thickness of the order of hundreds of nanometers and very small extends in direction parallel to the substrate. XRD results suggest that the dislocations along the crystallites are responsible for the c axis tilt dispersion.

The refractive indices of deposited aluminium nitride thin films are over 2 in the visible spectral range. These values are little bit smaller than those of a single crystal. Examining the differences between the refractive indices of the deposited thin films, it is observed that the AlN deposited on platinum has the highest refractive index, and therefore it is the denser one, result which agrees also with the XRD results. On the other hand, with this respect, the optical results are contradictory to XRD ones regarding the thin films deposited on Si and glass substrates. Therefore, the pure optical inspection does not give enough structural information.

A general characteristic of the films is the large microstrain which is related to the local defect structure within the crystallites. This is probably induced by ion bombardment during sputtering, but we found that it depends also on the substrate. However it is found that the microstrain decreases with thickness for the AlN film deposited onto Si, suggesting that the lattice defects at the interface are preponderant to those induced by ion bombardment. The AlN on glass shows the highest degree of lattice disorder, while that on Pt behaves similar as that with the same thickness deposited on Si, except that it has the maximum value of tensile strain along c axis. XRD results regarding micro- and macrostrain showed that a higher thickness is favourable to lattice relaxation, and also to the reduction of dislocation density resulting in a better c axis alignment. Therefore one can conclude that when using a low deposition temperature the increase of thickness leads to improved AlN film structure on Si or Pt supports. The microstructural properties obtained for the sputtered AlN films should offer an excellent piezoelectric coupling and be suitable for SAW and FBAR devices.

Acknowledgements: Thanks are due to Romanian Ministry of Education and Research for the *12-101/2008 GIGASABAR* scientific research project support.

References

- [1] A. Muller, G. Konstantinidis, D. Neculoiu, A. Dinescu, C. Morosanu, A. Stavrinidis, M. Dragoman, D. Vasilache, C. Buiculescu, I. Petrini, C. Anton, *Proceeding of the IEEE Microwave Conference APMC 2008. Asia-Pacific*, pages: 1-4 (2008).
- [2] A. Muller, G. Konstantinidis, D. Neculoiu, M. Dragoman, A. Dinescu, A. Stavrinidis, D. Vasilache, C. Morosanu, *IEEE 25th Convention of Electrical and Electronics Engineers in Israel*, Vols. 1 and 2, Book Series: *IEEE Convention of Electrical and Electronics Engineers in Israel*, pages: 561-564 (2008).
- [3] Ioffe data archive: <http://www.ioffe.rssi.ru/SVA/NSM/Semicond/AlN/index.html>
- [4] L. I. Berger, *Semiconductor materials*, CRC Press (1997).
- [5] S. Strite, H. Morkoc, *J. Vac. Sci. Technol. B* **10** 1237 (1992).
- [6] C. T. Leondes, *MEMS/NEMS: (1) Handbook Techniques and Applications Design Methods*, Springer (2006).
- [7] A. N. Red'kin, A. N. Gruzintsev, Z. I. Makovei, V. I. Tatsii, E. E. Yakimov, *Inorg. Mater.* **42**, 627 (2006).
- [8] R. Chandrasekaran, T. D. Moustakas, A. S. Ozcan, K. F. Ludwig, L. Zhou, D. J. Smith, *J. Appl. Phys.* **108**, 043501 (2010).
- [9] Y. Aota, S. Tanifuji, H. Oguma, S. Kameda, T. Takagi, K. Tsubouchi, *Proceeding of the IEEE Ultrasonics Symposium IUS 2008*, pages: 2197 – 2200 (2009).
- [10] T. Nagashima, M. Harada, H. Yanagi, Y. Kumagai, A. Koukitu, K. Takada, *J. Cryst. Growth* **300**, 42 (2007).

- [11] S. Simeonov, A. Szekeres, I. Minkov, S. Grigorescu, G. Socol, C. Ristoscu, I. N. Mihailescu, *J. Optoelectron. Adv. Mater.* **11**, 1292 (2009).
- [12] S. Bakalova, A. Szekeres, A. Cziraki, G. Huhn, K. Havancsak, S. Grigorescu, G. Socol, E. Axente, I. N. Mihailescu, R. Gavrilă, *J. Optoelectron. Adv. Mater.* **11**, 1479 (2009).
- [13] M. A. Auger, L. Vázquez, M. Jergel, O. Sánchez, J.M. Albella, *Surf. Coat. Technol.* **180–181**, 140 (2004).
- [14] V. Dumitru, C. Morosanu, V. Sandu, A. Stoica, *Thin Solid Films* **359**, 17 (2000).
- [15] G. F. Iriarte, *J. Vac. Sci. Technol. A* **28**, 193 (2010).
- [16] D. Neculoiu, A. Müller, G. Deligeorgis, A. Dinescu, A. Stavrinidis, D. Vasilache, A. M. Cismaru, G. E. Stan, G. Konstantinidis, *Electron. Lett.* **45**, 1196 (2009).
- [17] P. Kirsch, M. B. Assouar, O. Elmazria, V. Mortet, P. Alnot, *Appl. Phys. Lett.* **88**, 223504 (2006).
- [18] G. E. Stan, C. O. Morosanu, D. A. Marcov, I. Pasuk, F. Miculescu, G. Reumont, *Appl. Surf. Sci.* **255**, 9132 (2009).
- [19] R. E. Dinnebier, S. J. L. Billinge, *Powder Diffraction: Theory and Practice*, Royal Society of Chemistry (2008).
- [20] H. Fujiwara, *Spectroscopic Ellipsometry – Principles and Applications*, Wiley (2007).
- [21] A. C. Galca, E. S. Kooij, H. Wormeester, C. Salm, V. Leca, J. H. Rector, B. Poelsema, *J. Appl. Phys.* **94**, 4296 (2003).
- [22] L. Cauchy, *Bull. Sci. Math.* **14**, 6 (1830).
- [23] N. D. Scarisoreanu, A. C. Galca, L. Nedelcu, A. Ioachim, M. I. Toacsan, E. Morintale, S. D. Stoica, M. Dinescu, *Appl. Surf. Sci.* **256**, 6526 (2010).
- [24] D. A. G. Bruggeman, *Ann. Phys. Leipzig* **24**, 636 (1935).
- [25] E. D. Palik, *Handbook of Optical Constants of Solids* vol. III, Academic Press (1998).
- [26] A. Palmero, H. Rudolph, H.P.M. Habraken, *J. Appl. Phys.* **101**, 083307 (2007).
- [27] E.D. van Hattum, A. Palmero, W.M. Arnoldbik, H. Rudolph, F.H.P.M. Habraken, *Appl. Phys. Lett.* **91**, 171501 (2007).
- [28] M. Fujiki, M. Takahashi, S. Kikkawa, F. Kanamaru, *Journal of Materials Science Letters* **19**, 1625 (2000).